

Stationary planetary waves in the atmosphere of Mars during southern winter

D. P. Hinson,¹ R. J. Wilson,² M. D. Smith,³ and B. J. Conrath⁴

Received 14 June 2002; revised 14 October 2002; accepted 25 November 2002; published 30 January 2003.

[1] We report new observations of stationary planetary waves in the Southern Hemisphere of Mars by Mars Global Surveyor (MGS). We focus on a period during midwinter ($L_s = 134^\circ$ – 160°) when independent observations were acquired by two techniques. Radio occultation experiments sounded the atmosphere at essentially fixed latitude ($\sim 68^\circ$ S) and local time (~ 1030), yielding profiles of geopotential and temperature between the surface and the 9 Pa pressure level. Observations by the Thermal Emission Spectrometer (TES) included systematic limb sounding at nine discrete latitudes and two local times (~ 0200 and ~ 1500), yielding temperature profiles at pressures of 1–100 Pa. We supplemented these data with a simulation by a Mars general circulation model (MGCM), which provides an accurate synthesis of the observations. These stationary planetary waves have significant amplitudes at zonal wave numbers $s = 1$ and 2. The $s = 1$ component propagates vertically, as reflected by a westward tilt with increasing height in the geopotential and temperature fields and a net poleward eddy heat flux. The peak amplitude at $s = 1$ is ~ 1 km in geopotential height and ~ 7 K in temperature. The geopotential field of the $s = 2$ component is “barotropic” in character, which results through hydrostatic balance in a distinctive temperature field. The peak amplitude at $s = 2$ is ~ 700 m in geopotential height and 4–6 K in temperature. **INDEX TERMS:** 5445 Planetology: Solid Surface Planets: Meteorology (3346); 5409 Planetology: Solid Surface Planets: Atmospheres—structure and dynamics; 3346 Meteorology and Atmospheric Dynamics: Planetary meteorology (5445, 5739); 6225 Planetology: Solar System Objects: Mars; 6969 Radio Science: Remote sensing; **KEYWORDS:** Mars, atmosphere, meteorology, dynamics

Citation: Hinson, D. P., R. J. Wilson, M. D. Smith, and B. J. Conrath, Stationary planetary waves in the atmosphere of Mars during southern winter, *J. Geophys. Res.*, 108(E1), 5004, doi:10.1029/2002JE001949, 2003.

1. Introduction

[2] The general circulation of Mars is characterized by strong eastward winds in the winter hemisphere. The interaction of this flow with zonally varying topography excites stationary waves, which take the form of planetary (Rossby) waves for forcing at the largest horizontal scales [Gill, 1982, p. 525]. These waves can have a significant impact on the horizontal distribution of dust, the behavior of transient eddies, and the energy and momentum budgets at extratropical latitudes.

[3] Mars Global Surveyor (MGS) is providing the first unambiguous, vertically resolved measurements of station-

ary planetary waves on Mars. Banfield *et al.* [2003] have characterized their global structure and seasonal evolution through analysis of nadir observations by the MGS Thermal Emission Spectrometer (TES). Radio occultation experiments conducted as part of the MGS Radio Science (RS) investigation are providing a complementary view, offering a more detailed characterization at selected latitudes and seasons. Hinson *et al.* [2001] have reported initial RS results concerning the behavior of stationary waves at high northern latitudes during late spring.

[4] This paper reports new observations of stationary planetary waves in the Southern Hemisphere during midwinter. Our results compare favorably with those obtained by Banfield *et al.* [2003] at the same season and location but are complementary in several respects. First, we use a combination of RS and TES limb data, as opposed to TES nadir data, which enhances the vertical resolution and extends the vertical range of the results. Second, we exploit the RS data to obtain a unique measure of the geopotential field as well as the implied meridional winds and the poleward eddy heat flux. Finally, we quantify time variations in wave properties over shorter timescales than considered previously.

[5] Prior to MGS, much of our understanding of stationary planetary waves on Mars derived from numerical

¹Department of Electrical Engineering, Stanford University, Stanford, California, USA.

²National Oceanic and Atmospheric Administration (NOAA) Geophysical Fluid Dynamics Laboratory, Princeton University Forrestal Campus, Princeton, New Jersey, USA.

³Laboratory for Extraterrestrial Physics, National Aeronautics and Space Administration (NASA) Goddard Space Flight Center, Greenbelt, Maryland, USA.

⁴Center for Radiophysics and Space Research, Cornell University, Ithaca, New York, USA.

simulations [Zurek *et al.*, 1992; Hollingsworth and Barnes, 1996; Barnes *et al.*, 1996]. MGS has removed a significant source of uncertainty in these theoretical models by accurately defining the global topography [Smith *et al.*, 2001a]; new maps of surface thermal inertia are also available [Mellon *et al.*, 2000]. With the new results reported here, improved models can now be tested against direct observations. Toward this end, we evaluate the performance of a Mars general circulation model (MGCM) in simulating stationary planetary waves in the Southern Hemisphere.

[6] Where Banfield *et al.* [2003] have focused on obtaining a broad general description of stationary waves with complete seasonal and global coverage, the emphasis here is on deeper investigation of their behavior during midwinter of the Southern Hemisphere. The combination of RS and TES limb data with MGCM simulation yields a far more thorough characterization of such waves than has been obtained previously.

2. Experiment Description

[7] The MGS spacecraft is circling Mars in a low-altitude, polar, Sun-synchronous orbit with a period of ~ 2 hours. This mapping orbit provides daily global coverage for TES observations of thermal emission from the atmosphere and surface [Christensen *et al.*, 2001] as well as frequent opportunities for radio occultation experiments [Tyler *et al.*, 2001]. The atmospheric profiles obtained from these two instruments differ in both their basic properties and spatial distributions.

2.1. TES Profiles

[8] TES sounds the neutral atmosphere by observing thermal emission in the $15\ \mu\text{m}$ band of CO_2 . The inversion algorithm used for retrieving temperatures from these data is described by Conrath *et al.* [2000]. This procedure yields a profile of temperature versus pressure $T(p)$ over a pressure range that depends on the viewing geometry. In its nadir viewing mode, TES yields profiles that extend from the surface to a pressure of ~ 10 Pa. We are particularly interested in TES results at low pressures, so we focus primarily on profiles retrieved from limb observations. TES limb profiles have an accuracy of ~ 2 K and a pressure range of 1–100 Pa [Smith *et al.*, 2001b].

[9] Infrared limb sounding at Mars can in principle yield temperature profiles with a vertical resolution of ~ 5 km, or about half of a pressure scale height. However, the instrumental field of view must be correspondingly small to achieve this performance [e.g., McCleese *et al.*, 1992]. The field of view of TES is ~ 13 km for observations at the limb, and the vertical resolution of TES limb profiles is limited accordingly.

2.2. RS Profiles

[10] Radio occultation experiments sound the atmosphere by measuring its effect on the propagation of coherent microwave radiation. The method of data analysis is described by Hinson *et al.* [1999]. The basic result in the neutral atmosphere is a profile of number density versus radius $n(r)$ over the radial range $r_a < r < r_b$. The lower limit r_a lies within a few hundred meters of the surface, while the upper limit r_b is determined by data quality. Profiles of

pressure $p(r)$ and temperature $T(r)$ are derived from $n(r)$ by assuming hydrostatic balance, integrating vertically, and using the ideal gas law. For example,

$$T(r) = \frac{n_b T_b}{n(r)} + \frac{\bar{m}}{n(r)k} \int_r^{r_b} n(r') g(r') dr', \quad (1)$$

where \bar{m} is the average molecular mass of the gas mixture, k is the Boltzmann constant, and g is the acceleration of gravity. Integration extends to radius r_b where the density n_b is known but the temperature T_b is required as a boundary condition. Note that the term involving T_b in (1) is inversely proportional to density, so that the boundary condition has a significant effect on the profile only at high altitudes [cf. Hinson *et al.*, 2001, Figure 3].

[11] In the initial analysis of these RS data, we set T_b to 140 K at 10 Pa. The resulting profiles are available from the Planetary Data System (<http://pds.jpl.nasa.gov>) and a dedicated RS Web site (<http://nova.stanford.edu/projects/mgs/dmwr.html>). We later revised the profiles by adopting a boundary condition derived from TES limb data, as described in section 3. The results reported here are based on this second version of the RS profiles, in which T_b varies with longitude.

[12] These profiles have a diffraction limited vertical resolution of ~ 500 m [Karayel and Hinson, 1997; Hinson *et al.*, 1999]. The fractional uncertainties in T and p vary with pressure, with typical values of $\sim 4\%$ at 10 Pa and $\sim 0.6\%$ at 300 Pa. The radius scale inherent in the RS profiles has an uncertainty of a few meters, commensurate with the accuracy of the MGS orbit reconstructions [Lemoine *et al.*, 2001]. This allows accurate registration of the retrieved profiles within the gravity field of Mars, providing a measure of geopotential height on surfaces of constant pressure $Z(p)$.

2.3. Geometry

[13] We restrict our attention to the Southern Hemisphere at latitudes poleward of 35°S during midwinter ($L_s = 134^\circ - 160^\circ$, May and June 1999). This range of L_s includes the initial RS measurements after MGS began routine mapping operations. Occultations ceased at the end of this interval when the MGS orbit was nearly broadside to Earth [Tyler *et al.*, 2001, Figure 2].

[14] Figure 1 shows the distribution in local time, longitude, and latitude of the MGS data used here. This subset of TES limb data includes ~ 4800 profiles distributed evenly among nine discrete latitudes and two local times. The RS measurements comprise 442 profiles at latitudes of $67^\circ - 70^\circ\text{S}$ and a local time of ~ 1030 . These two sets of observations provide dense sampling in longitude at three distinct local times.

3. Method of Analysis

[15] This section describes the method used to identify and characterize stationary planetary waves. This task is complicated by the presence of thermal tides, which appear to be stationary in measurements at fixed local time due to aliasing [Forbes and Hagan, 2000; Wilson, 2000, 2002; Banfield *et al.*, 2003].

[16] Tidal modes can be divided into two basic categories, migrating (or Sun-synchronous) and nonmigrating, which

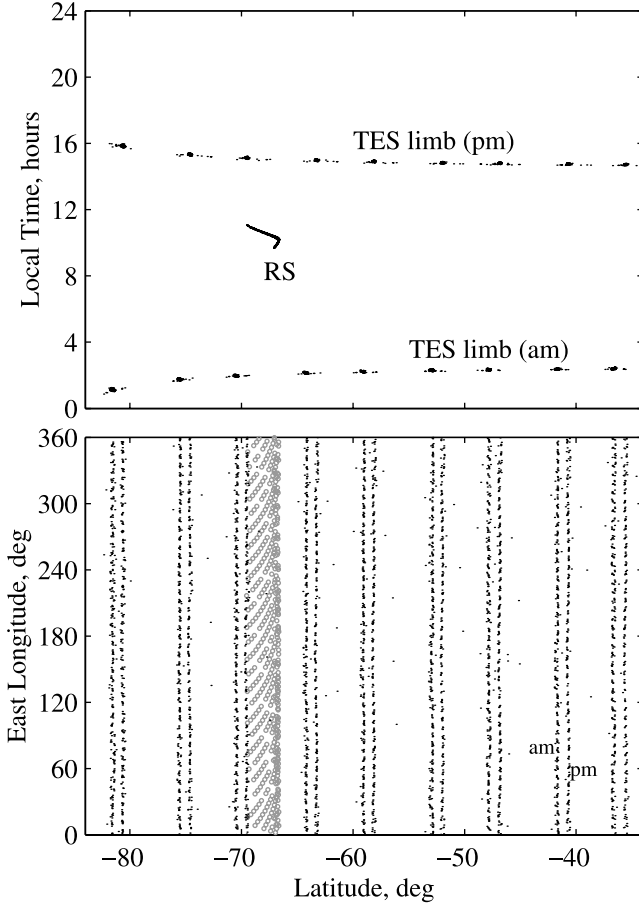


Figure 1. Distribution of RS and TES limb measurements in (top) local time and (bottom) longitude for $L_s = 134^\circ - 160^\circ$. The latitudes of the TES am (~ 0200) and pm (~ 1500) measurements differ by $\sim 1^\circ$.

have distinctly different effects on this analysis. When observed at fixed local time, migrating tides are independent of longitude. Hence they appear as a bias in zonal averages but do not interfere with measurements of zonal variations and stationary waves. In the case of nonmigrating tides, the aliased structure includes zonal variations that mimic the general appearance of a stationary wave.

3.1. RS Measurements

[17] According to the MGCM simulation described in section 5, nonmigrating tides are prominent within the tropics but are a minor component of the dynamics in the region considered here, particularly at the latitude of the RS measurements. This prediction is confirmed by the TES limb measurements presented in section 4.2 as well as TES nadir measurements at $L_s = 120^\circ - 140^\circ$ [Wilson, 2000, Figure 1]. We therefore ignore the effect of thermal tides in our analysis of the RS data.

[18] We characterized the quasi-stationary components of the geopotential $\langle Z \rangle$ and temperature $\langle T \rangle$ fields through least squares analysis of subsets of data spanning at least 10° in L_s (~ 19 days). This interval was selected to avoid interference from transient eddies, which also appear in these RS measurements [Hinson and Wilson, 2002]. In this case, the transient eddies have a period of ~ 2 solar days so

that their contribution to a 19-day average should be negligible.

[19] We modeled the quasi-stationary structure at fixed latitude, pressure, and local time as [Andrews *et al.*, 1987, p. 220]

$$\langle A \rangle \equiv \bar{A}(L_s) + A'(\lambda), \quad (2)$$

where λ is east longitude and A denotes either T or Z . The zonal mean \bar{A} is allowed to vary gradually with season, as represented by a second-order polynomial in L_s . The zonal variations A' include stationary zonal harmonics through wave number 4:

$$A' = \sum_{s=1}^4 A_s \cos[s\lambda - \alpha_s]. \quad (3)$$

Here, A_s and α_s are the amplitude and phase, respectively, of the component at zonal wave number s , where s is a dimensionless integer. Least squares solutions for A_s and α_s provide a convenient representation of stationary waves.

[20] Figure 2 illustrates this procedure using 209 samples of Z at 300 Pa spanning 19 days. When plotted versus L_s (Figure 2a) these data exhibit regular oscillations with an amplitude of ~ 200 m superimposed on a steady downward trend. These oscillations are stationary with respect to the surface, as shown in Figure 2b where the trend has been removed and the data are plotted versus longitude. The dashed line in Figure 2a and the solid line in Figure 2b show least squares solutions for \bar{Z} and Z' , respectively. During this interval \bar{Z} decreases by ~ 130 m. The components of Z' at wave numbers 1–4 have amplitudes of 128, 54, 46, and 23 m, respectively. Analogous results for T' appear in the study of Hinson and Wilson [2002, Figure 2a].

3.2. TES Measurements

[21] An extension of this procedure is possible with the TES data. Least squares solutions for $\langle T \rangle$ are obtained from subsets of data at fixed latitude, pressure, and local time. At each discrete latitude and pressure, an estimate for the stationary component of the temperature field is obtained by averaging results from the two local times,

$$\langle T \rangle_{stat} = (\langle T \rangle_{pm} + \langle T \rangle_{am})/2, \quad (4)$$

which largely removes the contribution from diurnal tides. Here, $\langle T \rangle_{pm}$ and $\langle T \rangle_{am}$ refer to solutions for $\langle T \rangle$ at local times of ~ 1500 and ~ 0200 , respectively. Similarly, an estimate for the diurnal tide is obtained from the difference,

$$\langle T \rangle_{tide} = (\langle T \rangle_{pm} - \langle T \rangle_{am})/2. \quad (5)$$

As in (2) and (3), both $\langle T \rangle_{stat}$ and $\langle T \rangle_{tide}$ are represented as a combination of zonal mean (\bar{T}_{stat} and \bar{T}_{tide}) and zonally varying (T'_{stat} and T'_{tide}) components.

[22] Note that the semidiurnal tide is removed by the difference in (5) but is preserved by the average in (4). However, its contribution to $\langle T \rangle_{stat}$ appears to be small as discussed in section 4.3. In addition, our MGCM simulation suggests that the semidiurnal and higher harmonics of the

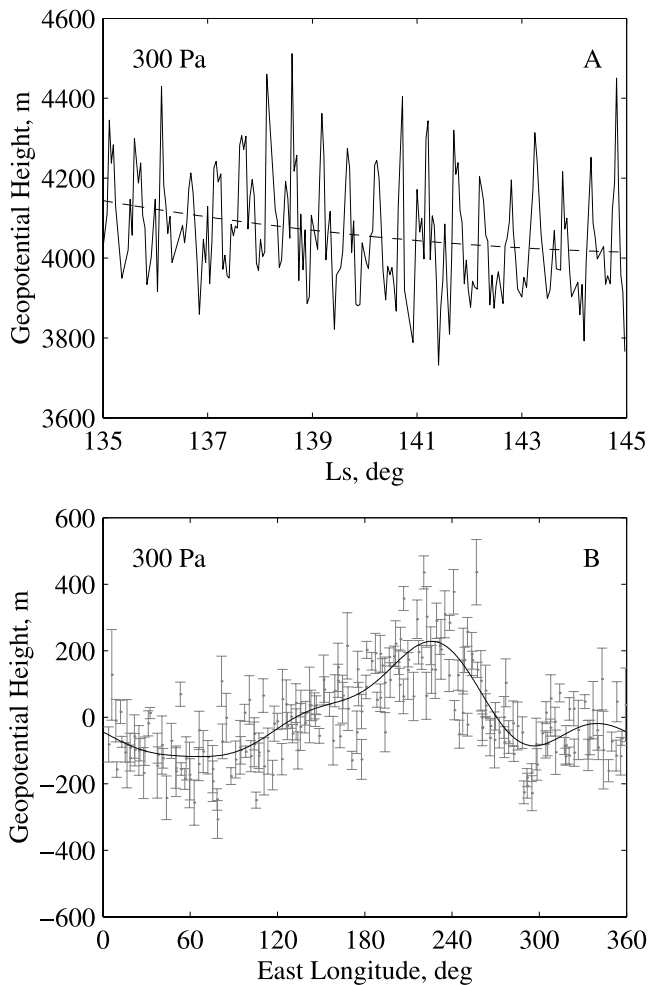


Figure 2. (a) Geopotential height at 300 Pa, ~ 3 km above the surface. The solid line shows RS measurements at 67° – 69° S. The dashed line is a least squares solution for the seasonal trend. (b) Zonal variations of the same data after the trend has been removed. The error bars correspond to one standard deviation, with an average value of 50 m. The solid line is an empirical model that includes stationary zonal harmonics through $s = 4$.

nonmigrating tides can safely be ignored for the data considered here.

[23] As an example, Figure 3 shows solutions for T'_{stat} and T'_{tide} derived from TES temperatures at 8.7 Pa for $L_s = 134^\circ$ – 160° . In this analysis, we included TES data from both 64° S and 70° S, the latitudes that bracket the RS measurements (cf. Figure 1). The $s = 1$ – 3 components of T'_{stat} have amplitudes of 6.1, 2.8, and 0.4 K, respectively, while the corresponding components of T'_{tide} have amplitudes of 0.5, 1.2, and 1.4 K. In both cases, the $s = 4$ component is negligible. At this pressure and latitude, the zonal spectrum of temperature variations is dominated by stationary waves with $s = 1$ and 2. Although the nonmigrating diurnal tides are relatively weak, they are the primary source of zonal variations at $s = 3$.

[24] We used this solution for $\langle T \rangle_{stat}$ at 8.7 Pa as a boundary condition for retrieving the second version of the RS profiles. Despite its simplicity, it captures much of

the variance of the TES data and represents a major improvement over the previous assumption of a zonally uniform T_b . All results reported here are based on this refined version of the RS profiles.

4. Results

[25] Stationary planetary waves have substantial amplitudes at $s = 1$ and 2 for the subsets of RS and TES limb data considered here. We limit discussion to these two components of the zonal spectrum.

[26] Our results should be viewed in the context of the broad description of stationary waves derived from TES nadir measurements by Banfield *et al.* [2003]. Within the Southern Hemisphere they report significant amplitudes at both $s = 1$ and 2 throughout the fall and winter seasons. There is a notable difference in the seasonal evolution of the two modes. The $s = 1$ amplitude has a distinct maximum around southern winter solstice ($L_s = 90^\circ$), while the $s = 2$ amplitude is relatively weak at the solstice and strongest in midfall and midwinter.

4.1. RS Measurements

[27] Although we analyzed several subsets of RS data, we will focus on results obtained from the interval $L_s = 150^\circ$ – 160° . There is little variation of latitude (66.7° – 67.1° S) or local time (0940–1020) within this set of measurements. We used least squares solutions for stationary zonal harmonics at 36 pressure levels to construct the cross section of Z' versus pressure and longitude that appears in Figure 4. Near the surface, the strongest zonal variations are at $s = 1$, with an amplitude of ~ 200 m, but the $s = 2$ component becomes more prominent with increasing height, resulting in ridge to trough variations of 1500 m at 10 Pa.

[28] Figure 5 shows the stationary component of the temperature field $\langle T \rangle$ obtained through least squares analysis of the same subset of data as in Figure 4. In constructing this figure we averaged \bar{T} over L_s , but there was little variation within this interval. Temperatures range from a minimum of ~ 137 K to a maximum of ~ 161 K.

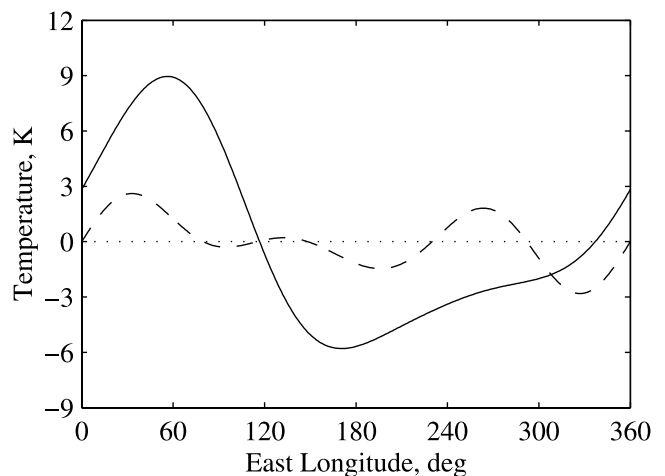


Figure 3. Zonal variations of temperature at 8.7 Pa derived from TES limb profiles for $L_s = 134^\circ$ – 160° . The solid and dashed lines show solutions for T'_{stat} and T'_{tide} , respectively. Each curve represents the average structure at 64° – 70° S.

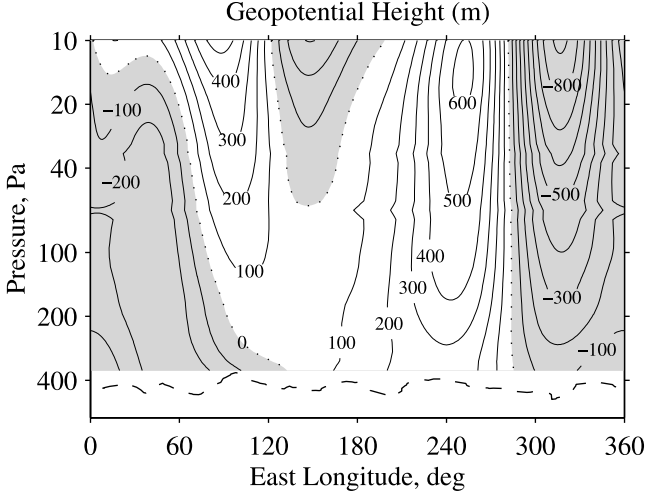


Figure 4. Stationary component of the RS geopotential field at 67°S , $L_s = 150^\circ\text{--}160^\circ$. The zonal average has been subtracted. The contour interval is 100 m and shading denotes negative values. The dashed line shows the pressure at the surface, which has an average value of 430 Pa.

[29] Figure 5 also shows the temperature deviations T' , analogous to the cross section of Z' in Figure 4. The temperature field contains comparable contributions at $s = 1$ and 2. Temperatures near the surface are relatively warm at 90°E and relatively cold at 330°E . The variations of T' at 10 Pa agree closely with T'_{stat} in Figure 3, which was used as a boundary condition in retrieving the RS profiles.

[30] We can gain additional insight by viewing the contributions from individual zonal harmonics. Figure 6 shows the $s = 1$ components of the RS measurements in Figures 4 and 5. The amplitude in Z' exceeds 190 m throughout the vertical range of Figure 6, with a peak amplitude of 290 m near 60 Pa. The amplitude in T' is ~ 6 K at low pressures and ~ 3 K near the surface, with smaller amplitudes at intermediate levels.

[31] Both the geopotential and temperature fields in Figure 6 tilt westward with increasing height. This implies that the vertical component of the group velocity is upward [Andrews *et al.*, 1987, pp. 179 and 185], consistent with forcing at the surface. As a consequence of this westward tilt, the maximum of T' lies roughly 90° west of the maximum of Z' throughout the vertical range of Figure 6 [Gill, 1982, p. 524].

[32] Figure 7 shows the $s = 2$ components of the RS measurements in Figures 4 and 5. In this case, the zonal variations of T' and Z' are nearly in phase, and both fields have only a slight westward tilt. The amplitude of T' is typically 2–3 K throughout this pressure range, while the amplitude of Z' increases steadily from 50 m near the surface to 460 m at 10 Pa, where it exceeds the amplitude at $s = 1$.

[33] Planetary waves conform closely to hydrostatic balance:

$$\frac{RT'}{H} = g_o \frac{\partial Z'}{\partial z}. \quad (6)$$

Here, H is the pressure scale height, R is the gas constant, g_o is the global average of gravity on the reference areoid, and

z is a log pressure vertical coordinate. When the temperature variations are vertically aligned, as in Figure 7, the amplitude of Z' grows steadily with increasing height.

[34] It is often assumed that extratropical planetary waves are in approximate geostrophic balance. The meridional wind speed v' can then be estimated from the zonal variations of Z' [e.g., Andrews *et al.*, 1987]:

$$v' \approx \frac{g_o}{f} \frac{\partial Z'}{\partial x}. \quad (7)$$

Here, x is eastward distance, $f \equiv 2\Omega \sin \phi$ (the Coriolis parameter), Ω is the rotation rate of Mars, and ϕ is latitude. Northward winds are positive by definition, and v' is poleward where $\partial Z'/\partial x > 0$. However, there are broad regions within the winter hemisphere of Mars where the flow deviates significantly from geostrophic balance, as discussed in section 6. (7) must therefore be used with caution. We apply it to the RS measurements at $67^\circ\text{--}70^\circ\text{S}$ only at pressures exceeding 60 Pa, where it appears to be accurate. We return to this point in section 6.

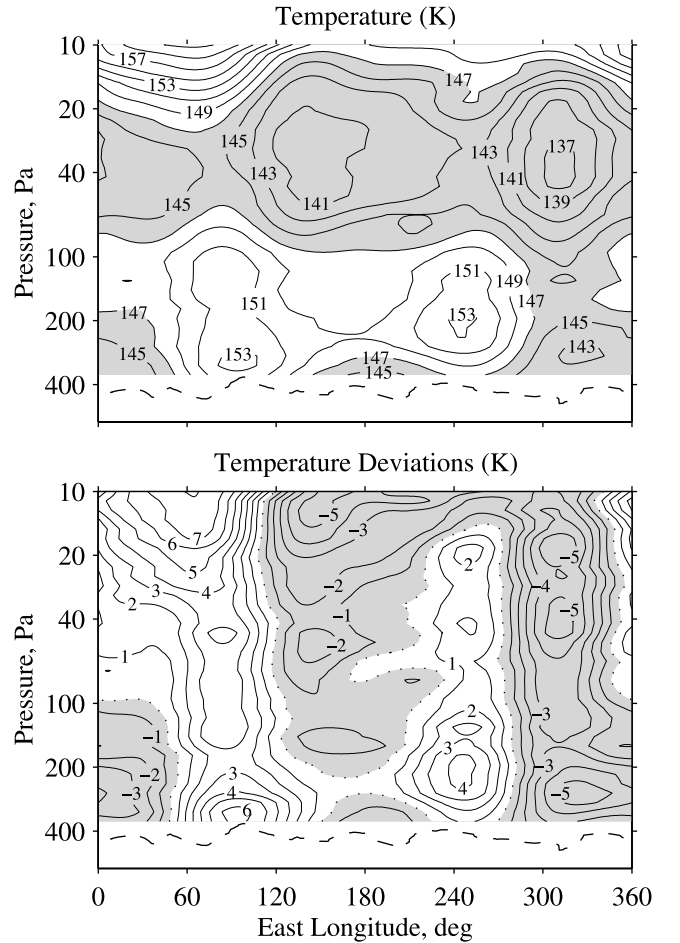


Figure 5. (Top) Stationary component of the RS temperature field at 67°S , $L_s = 150^\circ\text{--}160^\circ$. The contour interval is 2 K, and shading denotes temperatures <147 K. The dashed line shows the pressure at the surface. (Bottom) Zonal variations in the RS temperature field. The contour interval is 1 K and shading denotes negative values.

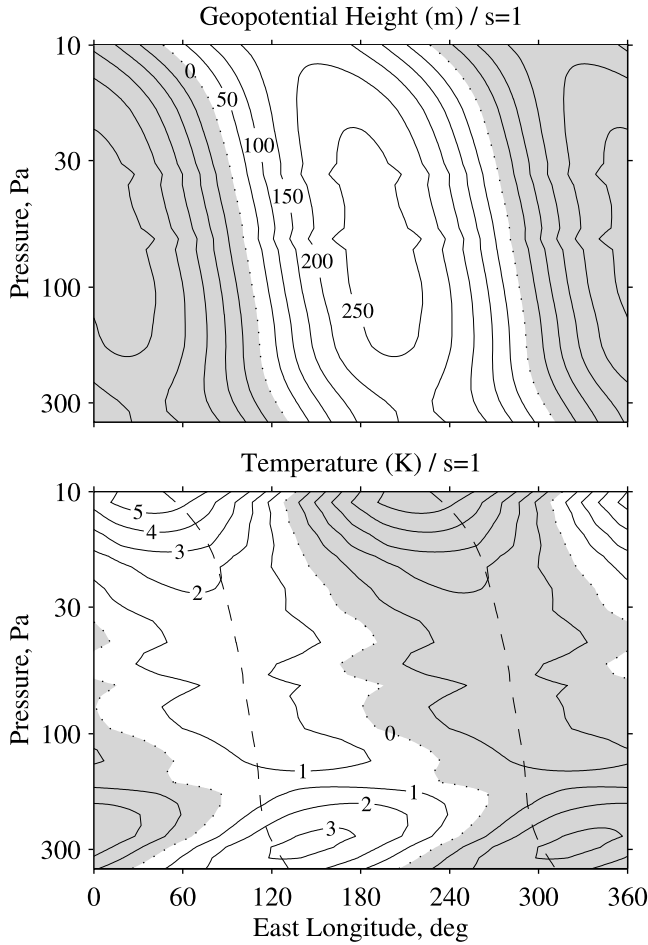


Figure 6. Wave 1 components of the RS measurements in Figures 4 and 5 at 67°S , $L_s = 150^\circ\text{--}160^\circ$. The contour intervals are (top) 50 m and (bottom) 1 K. The dashed lines in the lower panel show the locations where $Z' = 0$, which lie roughly midway between the locations where $T' = 0$.

[35] For the geopotential field in Figure 6, the strongest meridional winds occur where $Z' = 0$, which nearly coincides with the maxima and minima of T' . The amplitude of v' at $s = 1$ increases from 4 m s^{-1} near the surface to 6 m s^{-1} at 60 Pa. This configuration of the geopotential and temperature fields produces poleward advection of warm air and equatorward advection of cool air throughout the vertical range of Figure 6.

[36] The $s = 2$ geopotential field in Figure 7 implies a meridional wind field with an amplitude that increases from 2 m s^{-1} near the surface to 9 m s^{-1} at 60 Pa. As before, the strongest winds occur where $Z' = 0$, which in this case is near where $T' = 0$.

[37] The results in Figures 4–7 were derived from RS measurements at $L_s = 150^\circ\text{--}160^\circ$. While these are representative of the general structure of stationary waves observed throughout $L_s = 134^\circ\text{--}160^\circ$, significant variations occur within this interval. These changes are most notable within the lowest scale height above the surface at $s = 1$. For example, Figure 8 shows estimates of the zonal mean poleward eddy heat flux

$$\mathcal{F} \equiv -\rho c_p \overline{v'T'} \quad (8)$$

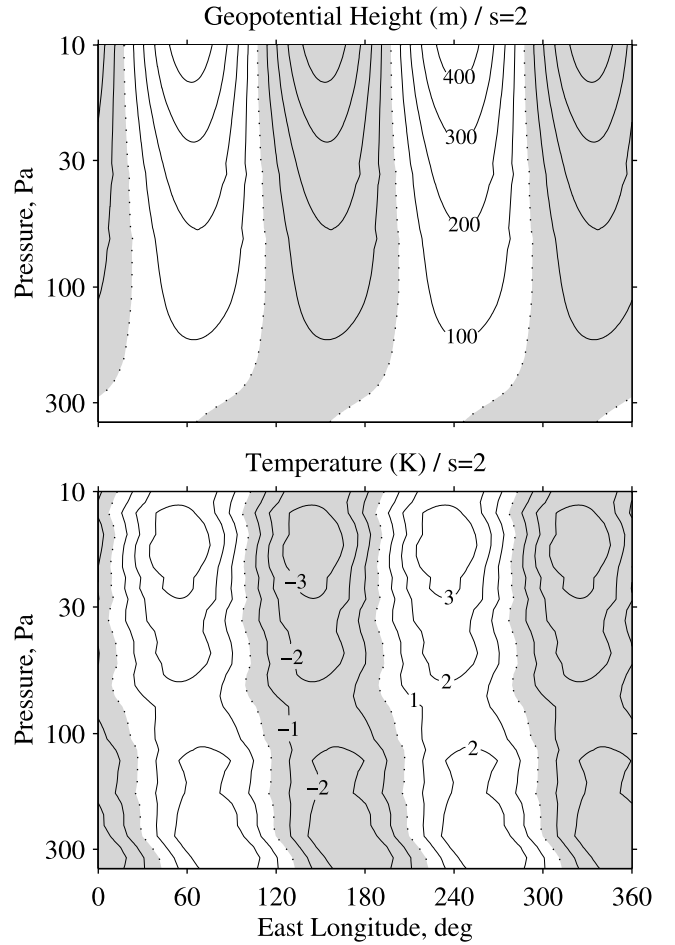


Figure 7. Wave 2 components of the RS measurements in Figures 4 and 5 at 67°S , $L_s = 150^\circ\text{--}160^\circ$. The contour intervals are (top) 100 m and (bottom) 1 K.

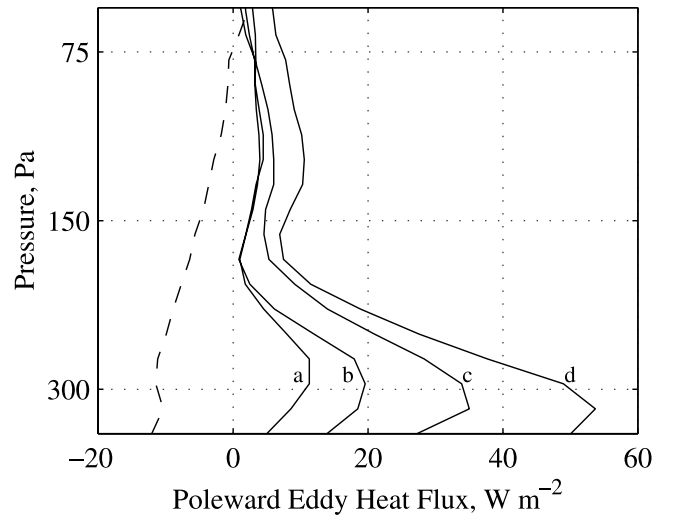


Figure 8. The zonal mean poleward eddy heat flux inferred from RS measurements. The solid lines show results at $s = 1$ from 10° intervals of L_s centered on (a) 140° , (b) 145° , (c) 150° , and (d) 155° . The dashed line shows results at $s = 2$ from $L_s = 135^\circ\text{--}160^\circ$. The average latitude of the measurements is 68°S .

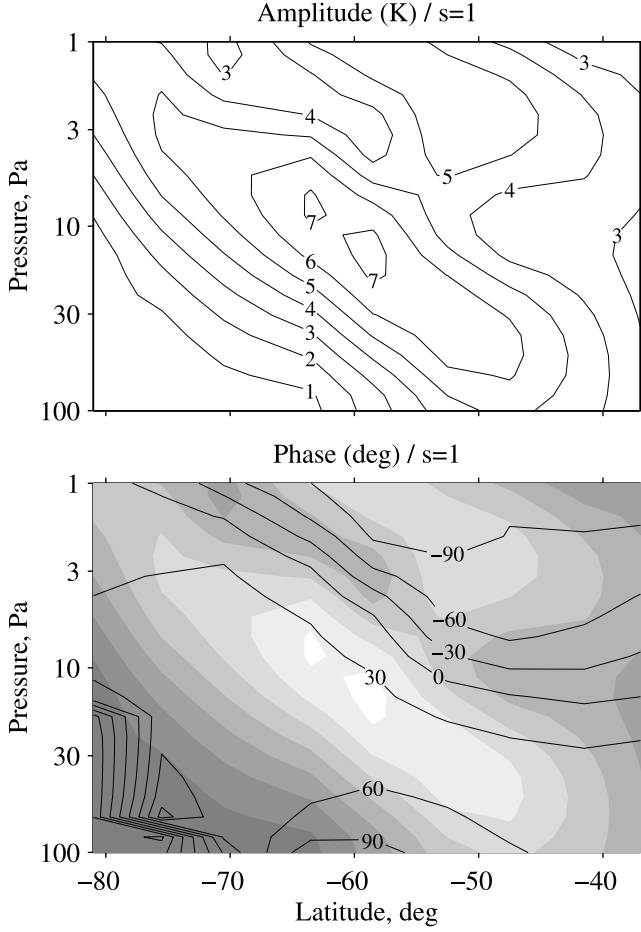


Figure 9. Contour plots of (top) amplitude and (bottom) phase for the $s = 1$ component of T'_{stat} derived from TES limb measurements at $L_s = 134^\circ$ – 160° . The contour intervals are (top) 1 K and (bottom) 30° . Amplitude is also shown by gray shading in the lower panel.

derived from RS measurements such as those in Figures 6 and 7. Here, ρ is the mass density and c_p is the specific heat at constant pressure. Near the 300 Pa pressure level, the $s = 1$ component of \mathcal{F} increases by a factor of ~ 5 during this interval, reaching a value of $\sim 50 \text{ W m}^{-2}$ at $L_s = 155^\circ$. The $s = 2$ component is smaller in magnitude and its variation with time is negligible.

[38] Transient eddies appear within this same set of RS measurements [Hinson and Wilson, 2002]. Although intermittent and confined in longitude, they have a much larger peak value of \mathcal{F} than these stationary waves. The relative importance of these eddy heat fluxes and their impact on the zonal mean temperature field are uncertain due to a well-known “nonacceleration theorem” [Andrews *et al.*, 1987, section 3.6]. Those issues can be addressed by using the RS results as constraints for MGCM simulation of winter dynamics in the Southern Hemisphere.

4.2. TES Measurements

[39] We now turn to TES limb data to gain a broader perspective on the temperature field, but we consider only the average structure for $L_s = 134^\circ$ – 160° .

[40] Figure 9 shows the $s = 1$ component of T'_{stat} , including latitude-height cross sections of both amplitude and phase as defined in (3). At $s = 1$ the phase corresponds to the east longitude of the maximum in temperature. The wave achieves its largest amplitude of $\sim 7 \text{ K}$ near 10 Pa and 60°S where the phase is $\sim 40^\circ$. Hence, the peak positive temperature perturbation lies above the southwest edge of Hellas. There is a notable secondary maximum of $\sim 5 \text{ K}$ centered near 3 Pa and 50°S . At constant latitude the phase moves steadily westward with increasing height. At constant pressure, the phase generally shifts eastward with increasing distance from the equator.

[41] Figure 10 shows the $s = 2$ component of T'_{stat} for the same time period. From (3), the phase must be divided by 2 to obtain the east longitude of the maximum in temperature. The amplitude of the $s = 2$ stationary wave has two distinct maxima of 4–5 K separated by an amplitude null sloping from upper left to lower right in Figure 10. In the region surrounding each maximum, the phase remains nearly constant. Its value in the lower left region is $+120^\circ$, so that peak positive temperatures occur at 60°E and 240°E , the longitudes of Hellas and Tharsis, respectively. The phase is -40° in the upper right region, corresponding to a longitude of

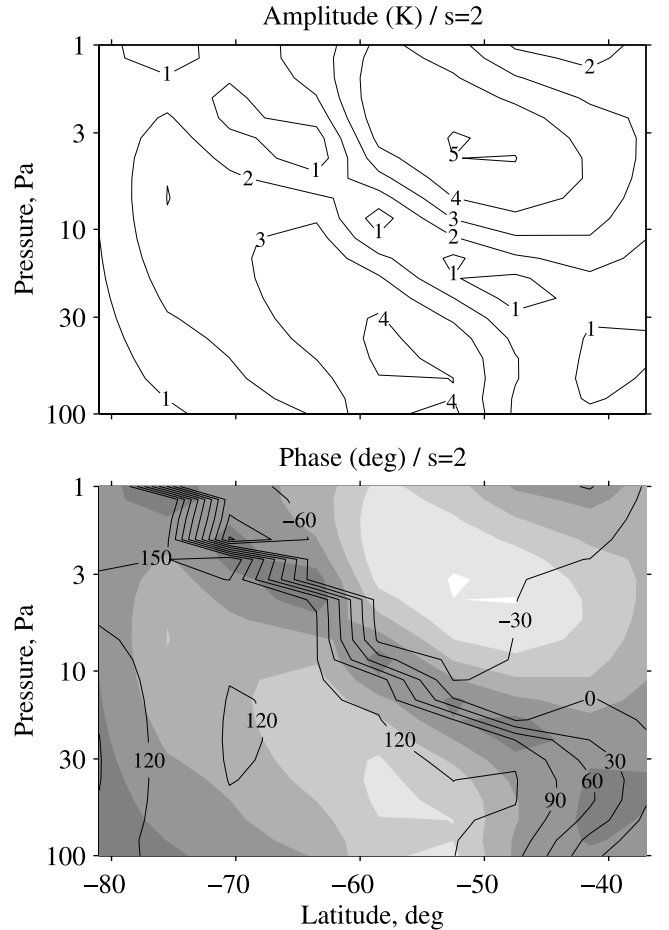


Figure 10. Contour plots of (top) amplitude and (bottom) phase for the $s = 2$ component of T'_{stat} derived from TES limb measurements at $L_s = 134^\circ$ – 160° . The contour intervals are (top) 1 K and (bottom) 30° . Amplitude is also shown by gray shading in the lower panel.

20°W. The phase transition between these regions is abrupt and coincides with the sloping band of weak amplitude.

[42] The portion of the thermal structure in Figures 9 and 10 at pressures exceeding 18 Pa appears in the TES nadir results reported by *Banfield et al.* [2003], but the structure at higher altitudes ($p < 18$ Pa) has not been observed previously. This illustrates the importance of TES limb measurements for providing a more complete characterization of these stationary waves, which have significant amplitudes at pressures less than 18 Pa.

[43] We also computed T'_{tide} from the TES limb measurements. The results confirm that the nonmigrating diurnal tides are a minor component of the dynamics over the range of latitudes and pressures in Figures 9 and 10. In particular, the amplitudes of both the $s = 1$ and 2 components are < 1 K at the location of the RS measurements.

4.3. Comparison of RS and TES Results

[44] *Banfield et al.* [2003] have analyzed TES nadir measurements spanning a full Martian year to characterize the global structure and seasonal evolution of stationary waves. The measurements extend from the surface to the 18 Pa pressure level, with a vertical resolution of ~ 1 scale height (or ~ 10 km) near the surface increasing to ~ 2 scale heights at low pressures. Their results in the Southern Hemisphere for $L_s = 135^\circ$ – 165° are generally consistent in both amplitude and phase with the RS and TES limb results reported here (Figures 6, 7, 9, and 10).

[45] These three data sets are highly complementary. TES nadir measurements offer nearly complete global and seasonal coverage of the lowest 3–4 scale heights of the atmosphere at modest vertical resolution. TES limb observations extend the characterization of stationary waves upward by nearly 3 scale heights to the 1 Pa pressure level, although spatial sampling is less dense than for the nadir observations [*Smith et al.*, 2001b]. The RS experiments described here are limited to essentially one latitude, but they provide much finer vertical resolution than TES and the only direct measure of the geopotential field. These attributes of the RS data are particularly important for characterizing the thermal structure and meridional winds within the lowest scale height above the surface.

[46] Figure 11 compares the RS and TES limb results reported here with TES nadir results derived by *Banfield et al.* [2003]. In computing T'_{stat} from the TES limb profiles we included data from both 64° S and 70° S, yielding an average latitude of 67° S.

[47] The RS and TES limb results in Figure 11 are generally consistent throughout the pressure range where both are available (10–100 Pa). This is to be expected at pressures near 10 Pa, where the TES limb data were used to prescribe a boundary temperature for retrieving the RS profiles, but the RS and TES limb temperatures are largely independent at pressures exceeding ~ 40 Pa. The phase estimates derived from these RS and TES limb measurements are essentially the same at both $s = 1$ and 2, and the amplitudes agree to within ~ 1 K. As semidiurnal tides would experience a phase shift of $\sim 180^\circ$ between the local times sampled by RS and TES (cf. Figure 1), their contribution to these measurements must be small.

[48] The difference in vertical resolution between the RS and TES observations is evident in Figure 11. For example

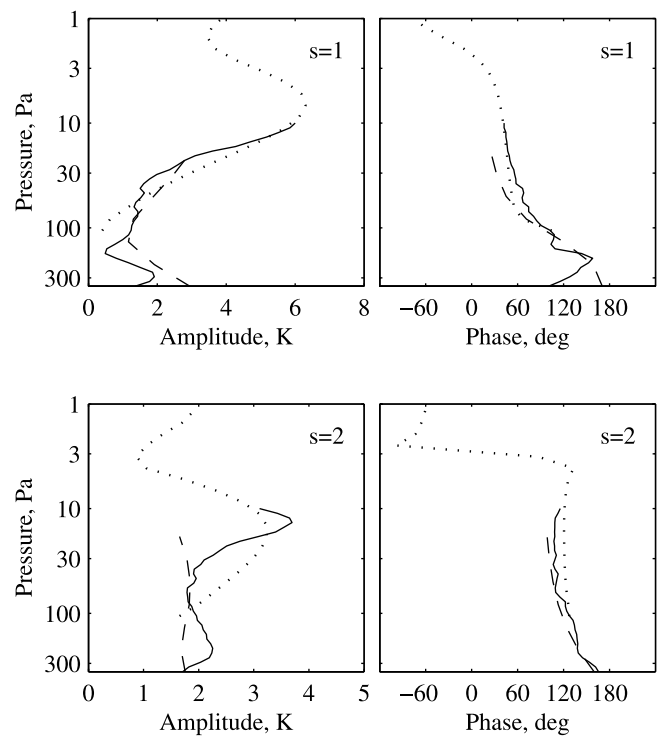


Figure 11. Thermal structure of stationary waves observed by RS and TES in southern winter. The panels show (top left) $s = 1$ amplitude, (top right) $s = 1$ phase, (bottom left) $s = 2$ amplitude, and (bottom right) $s = 2$ phase. The solid lines show RS results at 68° S for $L_s = 134^\circ$ – 160° . The dotted lines show TES limb results at 67° S for $L_s = 134^\circ$ – 160° . The dashed lines show results derived from TES nadir observations by *Banfield et al.* [2003] at 68° S for $L_s = 135^\circ$ – 165° .

the RS measurements reveal significant vertical variations in both amplitude and phase at $s = 1$, particularly at pressures exceeding 100 Pa, that are absent from the vertically smoothed TES measurements. In addition, the RS results contain a sharper peak in $s = 2$ amplitude at 10–20 Pa than appears in the TES results. On the other hand, the three estimates of $s = 2$ phase agree closely. This is reassuring, as differences of vertical resolution should have little effect when the phase is nearly uniform with height.

[49] Taken together, the RS and TES measurements provide a consistent characterization of these stationary waves that extends from the surface to the 1 Pa pressure level, a vertical range of ~ 6 scale heights.

5. MGCM Simulation

[50] The MGCM of the NOAA Geophysical Fluid Dynamics Laboratory (GFDL) has been developed as a tool for exploring the behavior of the Martian atmosphere and for interpreting observations by orbiting spacecraft and surface landers [*Wilson and Hamilton*, 1996; *Wilson*, 2000, 2002; *Wilson et al.*, 2002; *Richardson and Wilson*, 2002]. It has been used previously to investigate transient eddies that appear in the same subset of RS data considered here [*Hinson and Wilson*, 2002]. We now evaluate the performance of this MGCM in simulating the RS and

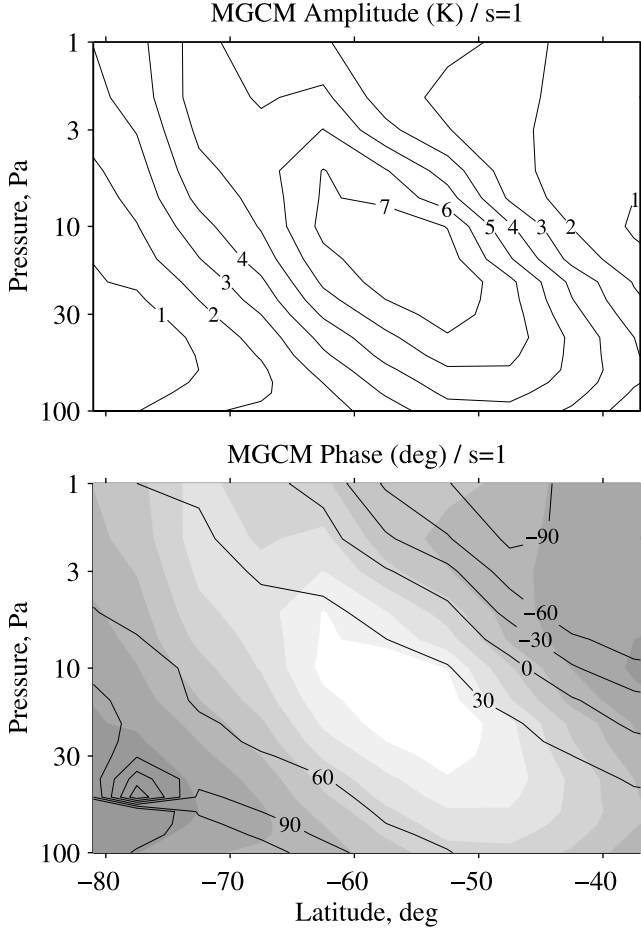


Figure 12. Temperature field of the $s = 1$ stationary wave simulated by the GFDL MGCM at $L_s = 150^\circ$. The two panels show contour plots of (top) amplitude and (bottom) phase, with contour intervals of 1 K and 30° , respectively. Amplitude is also shown by gray shading in the lower panel. This should be compared with the TES limb measurements in Figure 9.

TES limb observations of stationary waves during mid-winter of the Southern Hemisphere.

[51] We use a version of the MGCM with a horizontal resolution of 5° in latitude by 6° in longitude and 40 levels extending from the surface to an altitude of ~ 90 km. The dust distribution is prescribed and remains fixed throughout the simulation, unlike other versions of this MGCM where dust is redistributed by winds. The assumed dust distribution is similar to the model described by *Forget et al.* [1999], where the reference mixing ratio is horizontally uniform but the vertical distribution varies strongly with latitude. Dust is mixed to higher altitudes in the tropics than at the poles.

[52] We ran a series of MGCM simulations with different dust opacities and evaluated the results against a latitude-height cross section of zonal mean temperature constructed from TES nadir measurements. Near $L_s = 150^\circ$ we find best overall agreement between the simulated and observed temperature fields when the dust visible opacity is 0.2 in the tropics, consistent with estimates of the infrared opacity derived from TES data at this season [*Smith et al.*, 2001c].

[53] Moreover, the quality of the simulation also improves significantly when the model includes Rayleigh damping of the zonal winds at high altitudes. Its effect is similar to high-altitude gravity wave drag as implemented in another MGCM by *Forget et al.* [1999]. For simulations near $L_s = 150^\circ$, the addition of Rayleigh friction to the MGCM yields closer agreement with the temperatures observed at low pressures and high latitudes in the Southern Hemisphere, but it has little effect at other locations [cf. *Forget et al.*, 1999, Figure 9]. This augmentation of the MGCM also has an important effect on the simulated stationary waves as described below.

[54] The MGCM results shown here are derived from the “optimized” simulation that includes Rayleigh friction and a dust opacity of 0.2. We isolated the stationary waves in the simulation by first averaging over 10 days (at fixed location and local time) to remove transient eddies and then averaging over local time to remove thermal tides. We focus on the 10-day interval centered on $L_s = 150^\circ$.

[55] Figure 12 shows the $s = 1$ component of the simulated stationary waves, which compares favorably with the TES limb measurements in Figure 9. The simulation has

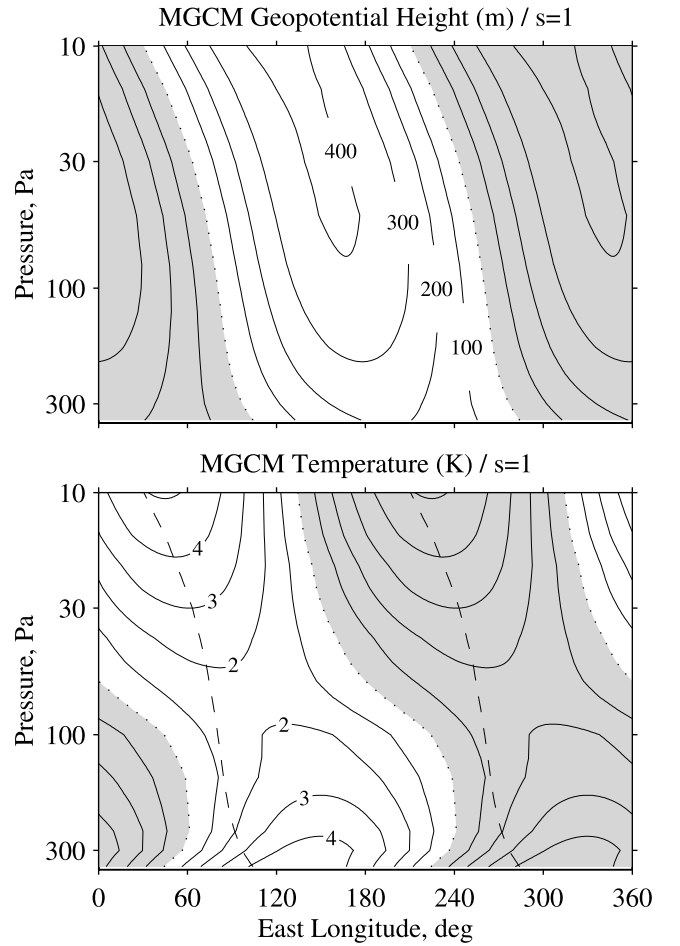


Figure 13. Geopotential and temperature fields of the $s = 1$ stationary wave simulated by the GFDL MGCM at 67.5°S , $L_s = 150^\circ$. The contour intervals are (top) 100 m and (bottom) 1 K. The locations where $Z' = 0$ are shown by dashed lines in the lower panel. This should be compared with the RS measurements in Figure 6.

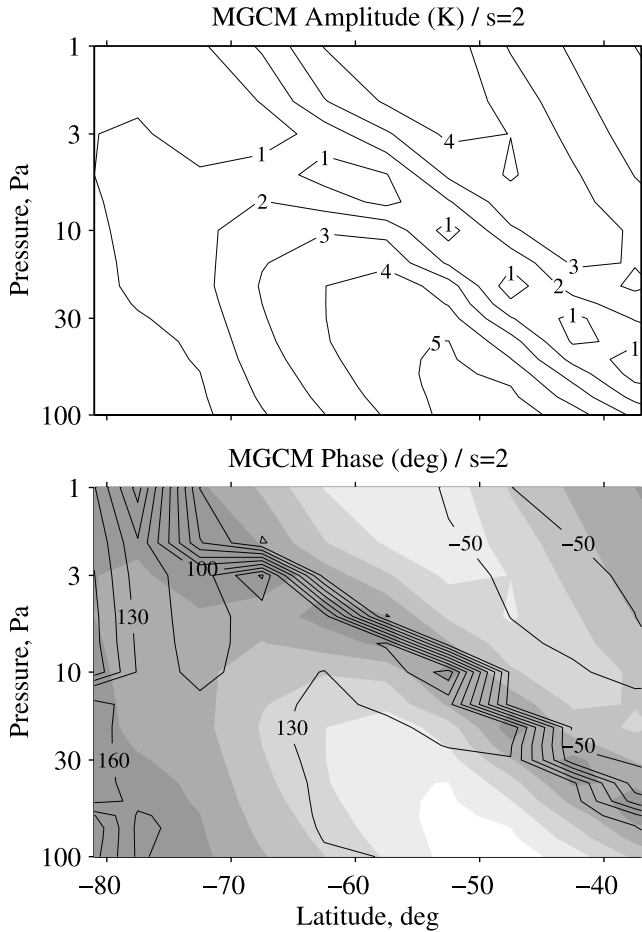


Figure 14. Temperature field of the $s = 2$ stationary wave simulated by the GFDL MGCM at $L_s = 150^\circ$. The two panels show contour plots of (top) amplitude and (bottom) phase, with contour intervals of 1 K and 30° , respectively. Amplitude is also shown by gray shading in the lower panel. This should be compared with the TES limb measurements in Figure 10.

a peak amplitude of ~ 8 K and a phase of 40° near 55°S and 15 Pa, close to the observations in each respect. In addition, the simulated $s = 1$ phase resembles the observations in the region surrounding the main peak, tilting westward with increasing height and eastward with increasing distance from the equator. Among the differences between Figures 9 and 12, only one seems serious. The secondary maximum observed near 3 Pa and 50°S is absent from the simulation. However, the simulation contains a suggestion of this type of structure at higher altitudes, as shown in Figure 16b.

[56] Figure 13 displays the $s = 1$ component of the simulated stationary waves in a format that allows comparison with the RS measurements in Figure 6. The simulation captures the main features of the data, including the local maximum in T' near the surface, both the absolute and relative phasing of the geopotential and temperature fields, and the westward tilt with increasing height in both fields. The amplitude in temperature of the simulated wave is ~ 1 K larger than observed, which leads through hydrostatic balance to a somewhat larger amplitude in geopotential as well. However, the overall structure

in the simulation bears a strong resemblance to the measurements.

[57] Figure 14 shows the $s = 2$ component of the simulated stationary waves, which closely resembles the measurements in Figure 10. Both figures contain two distinct maxima in amplitude separated by an amplitude null extending from upper left to lower right. An abrupt phase transition occurs within this band of weak amplitude, but there is little phase variation with pressure or latitude outside the band. The simulated and observed $s = 2$ stationary waves are aligned to within 5° – 10° in longitude (10° – 20° in phase).

[58] Figure 15 shows the zonal structure of the simulated stationary waves at $s = 2$, and we find good agreement with the corresponding RS measurements in Figure 7. Within the lowest scale height the measured amplitudes exceed the simulated values by ~ 1 K and ~ 50 m, but the simulation and the observations are essentially the same at pressures less than 100 Pa.

[59] Figure 16 shows the overall structure of the simulated stationary waves, which accurately reflects the main features of the RS and TES limb measurements in Figures 6,

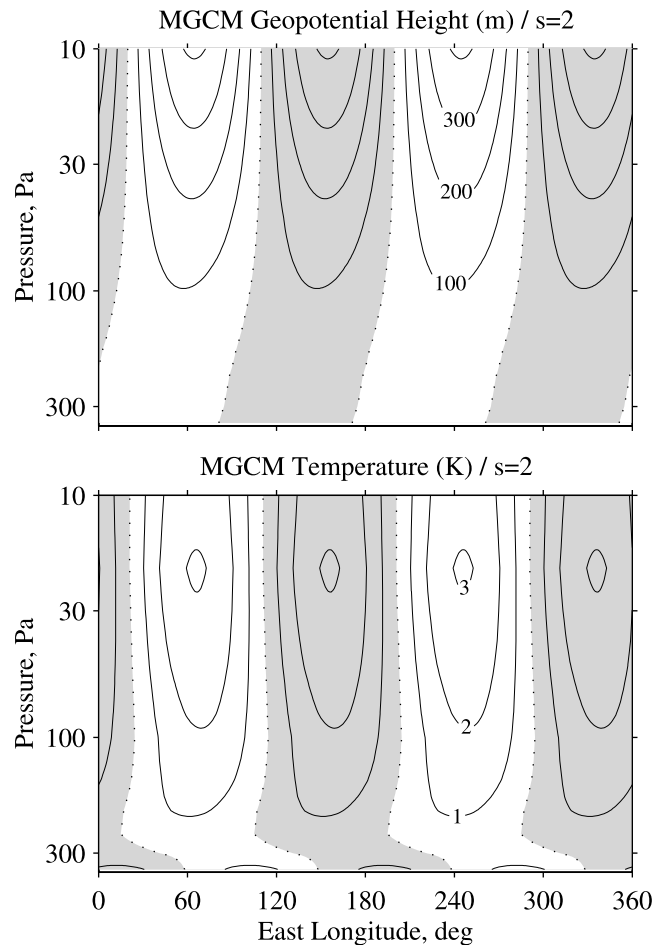


Figure 15. Geopotential and temperature fields of the $s = 2$ stationary wave simulated by the GFDL MGCM at 67.5°S , $L_s = 150^\circ$. The contour intervals are (top) 100 m and (bottom) 1 K. This should be compared with the RS measurements in Figure 7.

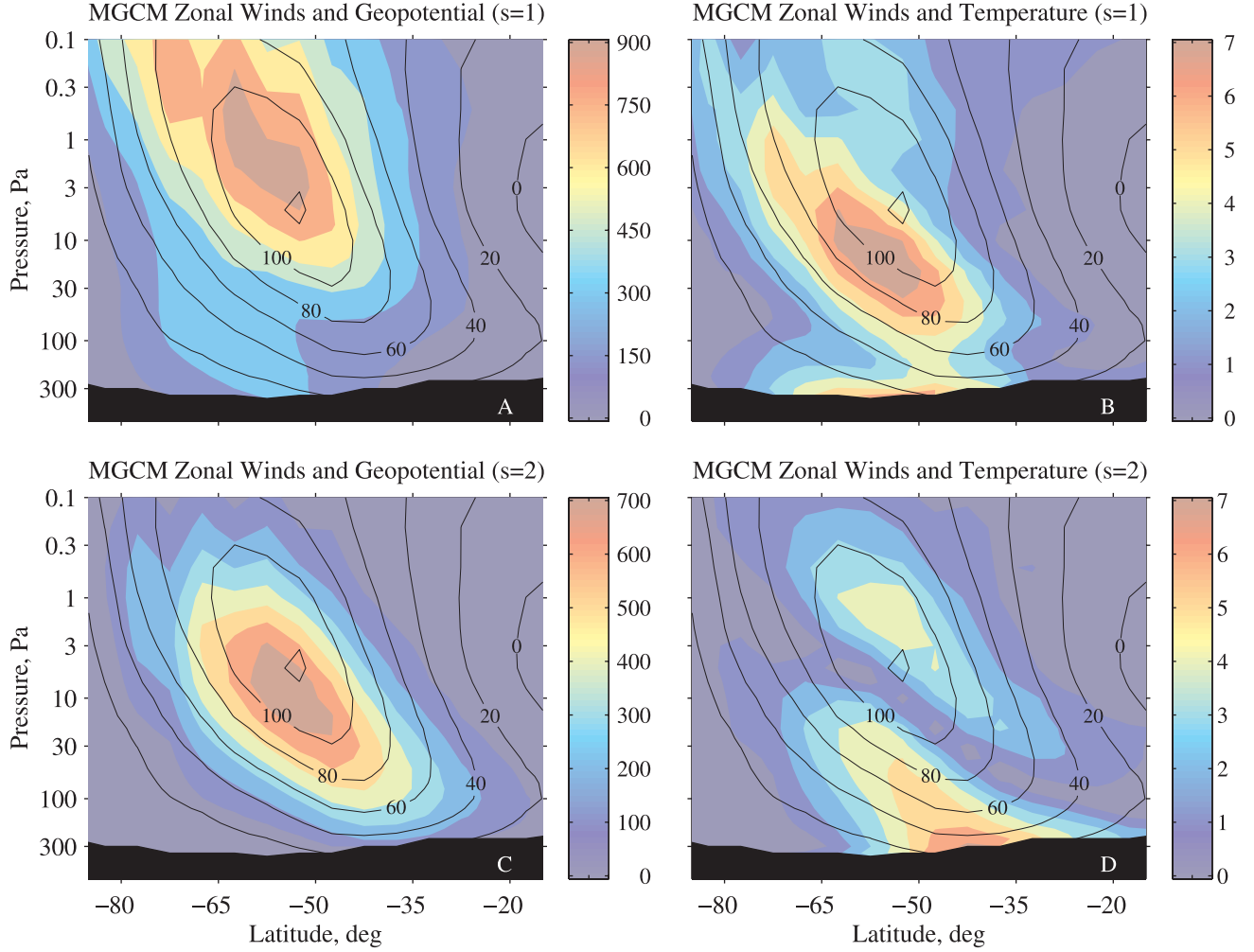


Figure 16. The black lines in each panel show contours of the mean zonal wind field at intervals of 20 m s^{-1} . The amplitude of stationary waves is indicated by color shading for (a) geopotential height at $s = 1$, (b) temperature at $s = 1$, (c) geopotential height at $s = 2$, and (d) temperature at $s = 2$. All results are from a simulation by the GFDL MGCM at $L_s = 150^\circ$. The contour intervals are (a) 150 m, (b) 1 K, (c) 100 m, and (d) 1 K. Results are shown only at pressures that remain above the surface at all longitudes.

7, 9, and 10. This figure provides a convenient framework for discussing additional aspects of wave behavior.

[60] The simulated zonal-mean zonal winds \bar{u} include an eastward jet in the Southern (winter) Hemisphere, as shown in Figure 16, with a peak wind speed of $\sim 120 \text{ m s}^{-1}$. This simulated zonal wind field compares favorably with the cross section of gradient winds derived from TES data at $L_s = 135^\circ$ by Smith *et al.* [2001b, Plate 5]. Figure 16 reveals a strong correlation between the contours of \bar{u} and Z' (Figures 16a and 16c), which slope poleward with increasing height. This correlation reflects the strong influence of the zonal wind field on the propagation of planetary waves [e.g., Andrews *et al.*, 1987, section 4.5].

[61] The $s = 1$ stationary wave in Figure 16a extends to pressures less than 0.1 Pa, or more than 8 scale heights above the surface, with a peak amplitude of $\sim 1 \text{ km}$ near 1 Pa and 60°S . The amplitude in temperature at $s = 1$ (Figure 16b) is particularly large in two distinct regions. The first lies along the poleward flank of the zonal jet, while the second is narrowly confined near the surface. Both regions are evident in the RS measurements at 67°S (Figures 6 and

11). Near the surface the peak positive temperature perturbations occur in a band that extends from 70°E at 40°S , above Hellas, to 135°E at 70°S . These locations are 80° and 60° west, respectively, of the maximum in geopotential height near the surface, resulting in a significant poleward eddy heat flux at low altitudes (cf. Figure 8).

[62] The $s = 2$ geopotential field is “barotropic” in character (Figure 16c). Its phase remains very close to 130° at all pressures and latitudes where Z' is appreciable. In the region below the null of T' in Figure 16d, T' and Z' are nearly in phase so that Z' grows steadily with increasing height (cf. Figures 7 and 15). The $s = 2$ geopotential exceeds 700 m within a sloping band that coincides with the null of T' . At higher altitudes, Z' and T' are 180° out of phase and Z' decays with increasing height, as expected from (6). The amplitude in temperature is largest near the surface, exceeding 6 K at 35° – 50°S , consistent with TES nadir measurements at this season [Banfield *et al.*, 2003, Figure 10]. The contours of both Z' and T' at $s = 2$ give the impression of wave energy emanating from the surface at latitudes of roughly 20° – 50°S and traveling upward and poleward

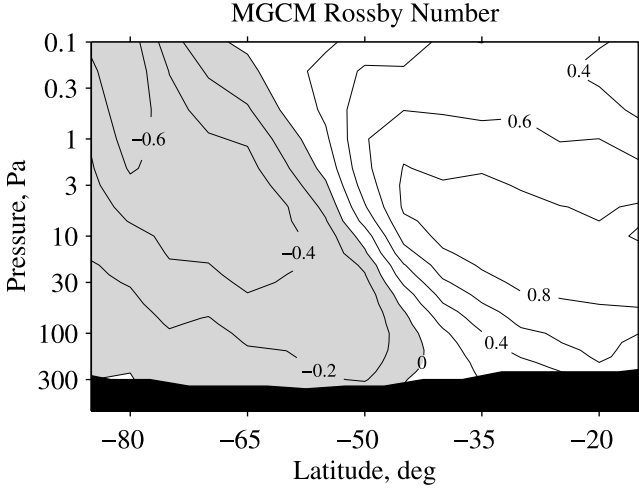


Figure 17. Contour plot of Ro computed from the simulated zonal wind field in Figure 16. The contour interval is 0.2, and shading denotes negative values.

along the axis of the eastward jet. The peak positive perturbations of Z' occur at longitudes of 65°E and 245°E , so that the geopotential disturbance is in phase with the topography near Tharsis but out of phase near Hellas.

6. Discussion

[63] The $s = 1$ and 2 components of the simulated stationary waves reside in somewhat different regions of Figure 16. Hence, the two modes are sensitive to different aspects of the zonal wind field. For this reason Rayleigh friction, which reduces \bar{u} at high altitudes, has a dramatically different effect on the two components. In its absence, the amplitude at $s = 1$ increases by a factor of ~ 2 while the amplitude at $s = 2$ is essentially unchanged. By adding Rayleigh friction to the MGCM, we were able to assess the sensitivity of the stationary waves to subtle changes in the zonal mean temperature and zonal wind fields, leading to a much improved simulation.

[64] Large deviations from geostrophic balance occur in the vicinity of the intense jet that appears in Figure 16. These effects can be quantified by considering the case of planetary waves within a basic zonal flow $\bar{u}(\phi, z)$. Retaining the leading terms in the zonal momentum equation [e.g., Andrews *et al.*, 1987, p. 114]:

$$\left(f + \frac{\bar{u} \tan \phi}{r_m} - \frac{\partial \bar{u}}{\partial y}\right) v' = g_\phi \frac{\partial Z'}{\partial x}, \quad (9)$$

where y is northward distance and r_m is the radius of Mars. This expression reduces to geostrophic balance, as in (7), when two conditions are satisfied. First,

$$\frac{\bar{u}}{2 \Omega r_m \cos \phi} \ll 1. \quad (10)$$

The second condition can be expressed as

$$|Ro| \ll 1, \quad (11)$$

where the Rossby number

$$Ro \equiv \frac{1}{f} \frac{\partial \bar{u}}{\partial y}. \quad (12)$$

[65] It is widely recognized that the strongest winds in the winter hemisphere of Mars routinely violate the first condition. This is true for the simulated winds in Figure 16, where the left-hand side of (10) approaches 0.5 within the core of the jet. For this reason, geostrophic balance gives way to gradient wind balance in regions where \bar{u} is particularly large [e.g., Conrath *et al.*, 2000; Smith *et al.*, 2001b; Banfield *et al.*, 2003].

[66] The limitation imposed by the second condition is more serious, as shown in Figure 17. The magnitude of Ro exceeds 0.4 within broad regions on both the poleward and equatorward flanks of the jet, with a local maximum of +0.9 at 30°S and 10 Pa. Significant departures from geostrophic balance occur throughout much of Figure 17.

[67] However, these results suggest that geostrophic balance is a good approximation to (9) at $67^\circ\text{--}70^\circ\text{S}$ for pressures exceeding 60 Pa, where $|Ro| < 0.25$ and (10) is easily satisfied. In section 4.1, we applied (7) to RS measurements within this region, and the resulting estimates for v' and \mathcal{F} should be reliable.

[68] Quasi-geostrophic theory is the traditional framework for theoretical models of planetary waves. One condition for its validity is that $|Ro| \ll 1$, which ensures that the nonlinear part of the ageostrophic velocity is small compared with the geostrophic velocity [Andrews *et al.*, 1987, p. 120; Gill, 1982, p. 498]. Hence the results in Figure 17 suggest that the dynamics of the winter jet are generally not well suited to analysis using quasi-geostrophic theory. Standard diagnostics, such as the quasi-geostrophic index of refraction [e.g., Barnes *et al.*, 1996; Banfield *et al.*, 2003], should be used with caution under these conditions.

[69] **Acknowledgments.** Funding for this work was provided by the MGS Project and the NASA Mars Data Analysis Program. We are grateful to Jeff Hollingsworth for many useful discussions, to Don Banfield for providing selected results from his analysis of TES nadir observations, and to the RS and TES teams of the MGS Project led by G. L. Tyler and P. R. Christensen, respectively.

References

- Andrews, D. G., J. R. Holton, and C. B. Leovy, *Middle Atmosphere Dynamics*, 489 pp., Academic, San Diego, Calif., 1987.
- Banfield, D., B. J. Conrath, J. Pearl, M. D. Smith, P. R. Christensen, and R. J. Wilson, Forced waves in the Martian atmosphere from MGS TES nadir data, *Icarus*, in press, 2003.
- Barnes, J. R., R. M. Haberle, J. B. Pollack, H. Lee, and J. Schaeffer, Mars atmospheric dynamics as simulated by the NASA Ames general circulation model, 3, Winter quasi-stationary eddies, *J. Geophys. Res.*, **101**, 12,753–12,776, 1996.
- Christensen, P. R., et al., The Mars Global Surveyor Thermal Emission Spectrometer experiment: Investigation description and surface science results, *J. Geophys. Res.*, **106**, 28,823–28,871, 2001.
- Conrath, B. J., J. C. Pearl, M. D. Smith, W. C. Maguire, P. R. Christensen, S. Dason, and M. S. Kaelberer, Mars Global Surveyor Thermal Emission Spectrometer (TES) observations: Atmospheric temperatures during aerobraking and science phasing, *J. Geophys. Res.*, **105**, 9509–9519, 2000.
- Forbes, J. M., and M. E. Hagan, Diurnal Kelvin wave in the atmosphere of Mars: Towards an understanding of “stationary” density structures observed by the MGS accelerometer, *Geophys. Res. Lett.*, **27**, 3563–3566, 2000.
- Forget, F., F. Hourdin, R. Fournier, C. Hourdin, O. Talagrand, M. Collins, S. R. Lewis, P. L. Read, and J.-P. Huot, Improved general circulation

- models of the Martian atmosphere from the surface to above 80 km, *J. Geophys. Res.*, **104**, 24,155–24,176, 1999.
- Gill, A. E., *Atmosphere–Ocean Dynamics*, 662 pp., Academic, San Diego, Calif., 1982.
- Hinson, D. P., and R. J. Wilson, Transient eddies in the Southern Hemisphere of Mars, *Geophys. Res. Lett.*, **29**, 1154, doi:10.1029/2001GL014103, 2002.
- Hinson, D. P., R. A. Simpson, J. D. Twicken, G. L. Tyler, and F. M. Flasar, Initial results from radio occultation measurements with Mars Global Surveyor, *J. Geophys. Res.*, **104**, 26,997–27,012, 1999.
- Hinson, D. P., G. L. Tyler, J. L. Hollingsworth, and R. J. Wilson, Radio occultation measurements of forced atmospheric waves on Mars, *J. Geophys. Res.*, **106**, 1463–1480, 2001.
- Hollingsworth, J. L., and J. R. Barnes, Forced stationary planetary waves in Mars's winter atmosphere, *J. Atmos. Sci.*, **53**, 428–448, 1996.
- Karayel, T. E., and D. P. Hinson, Sub-Fresnel-scale vertical resolution in atmospheric profiles from radio occultation, *Radio Sci.*, **32**, 411–423, 1997.
- Lemoine, F. G., D. E. Smith, D. D. Rowlands, M. T. Zuber, G. A. Neumann, D. S. Chinn, and D. E. Pavlis, An improved solution of the gravity field of Mars (GMM-2B) from Mars Global Surveyor, *J. Geophys. Res.*, **106**, 23,359–23,376, 2001.
- McCleese, D. J., R. D. Haskins, J. T. Schofield, R. W. Zurek, C. B. Leovy, D. A. Paige, and F. W. Taylor, Atmosphere and climate studies of Mars using the Mars Observer Pressure Modulator Infrared Radiometer, *J. Geophys. Res.*, **97**, 7735–7757, 1992.
- Mellon, M. T., B. M. Jakosky, H. H. Kieffer, and P. R. Christensen, High-resolution thermal inertia mapping from the Mars Global Surveyor Thermal Emission Spectrometer, *Icarus*, **148**, 437–455, 2000.
- Richardson, M. I., and R. J. Wilson, Investigation of the nature and stability of the Martian seasonal water cycle with a general circulation model, *J. Geophys. Res.*, **107**, 5031, doi:10.1029/2001JE001536, 2002.
- Smith, D. E., et al., Mars Orbiter Laser Altimeter: Experiment summary after the first year of global mapping of Mars, *J. Geophys. Res.*, **106**, 23,689–23,722, 2001a.
- Smith, M. D., J. C. Pearl, B. J. Conrath, and P. R. Christensen, Thermal Emission Spectrometer results: Mars atmospheric thermal structure and aerosol distribution, *J. Geophys. Res.*, **106**, 23,929–23,945, 2001b.
- Smith, M. D., J. C. Pearl, B. J. Conrath, and P. R. Christensen, One Martian year of atmospheric observations by the Thermal Emission Spectrometer, *Geophys. Res. Lett.*, **28**, 4263–4266, 2001c.
- Tyler, G. L., G. Balmino, D. P. Hinson, W. L. Sjogren, D. E. Smith, R. A. Simpson, S. W. Asmar, P. Priest, and J. D. Twicken, Radio Science observations with Mars Global Surveyor: Orbit insertion through one Mars year in mapping orbit, *J. Geophys. Res.*, **106**, 23,327–23,348, 2001.
- Wilson, R. J., Evidence for diurnal period Kelvin waves in the Martian atmosphere from Mars Global Surveyor TES data, *Geophys. Res. Lett.*, **27**, 3889–3892, 2000.
- Wilson, R. J., Evidence for nonmigrating thermal tides in the Mars upper atmosphere from the Mars Global Surveyor Accelerometer experiment, *Geophys. Res. Lett.*, **29**, 1120, doi:10.1029/2001GL013975, 2002.
- Wilson, R. J., and K. Hamilton, Comprehensive model simulation of thermal tides in the Martian atmosphere, *J. Atmos. Sci.*, **53**, 1290–1326, 1996.
- Wilson, R. J., D. Banfield, B. J. Conrath, and M. D. Smith, Traveling waves in the Northern Hemisphere of Mars, *Geophys. Res. Lett.*, **29**(14), 1684, doi:10.1029/2002GL014866, 2002.
- Zurek, R. W., J. R. Barnes, R. M. Haberle, J. B. Pollack, J. E. Tillman, and C. B. Leovy, Dynamics of the atmosphere of Mars, in *Mars*, edited by H. H. Kieffer, B. M. Jakosky, C. W. Snyder, and M. S. Matthews, pp. 835–933, Univ. of Ariz. Press, Tucson, 1992.

B. J. Conrath, Center for Radiophysics and Space Research, Cornell University, Ithaca, NY 14853, USA. (barney@chryse.gsfc.nasa.gov)

D. P. Hinson, Department of Electrical Engineering, Stanford University, 350 Serra Mall, Stanford, CA 94305-9515, USA. (hinson@nimbus.stanford.edu)

M. D. Smith, National Aeronautics and Space Administration (NASA) Goddard Space Flight Center, Code 693, Greenbelt, MD 20771, USA. (Michael.D.Smith.1@gsfc.nasa.gov)

R. J. Wilson, National Oceanic and Atmospheric Administration (NOAA) Geophysical Fluid Dynamics Laboratory, Princeton University Forrestal Campus, P.O. Box 308, Princeton, NJ 08542, USA. (rjw@gfdl.noaa.gov)